ACS APPLIED ENERGY MATERIALS

Open Access

This article is licensed under CC-BY 4.0

www.acsaem.org

Article

Correlation between Fe/Mn/Ni Ratio and Structural Properties in P2-$Na_{2/3}Mn_{2/3}Fe_{1/3-x}Ni_xO_2$ (x = 0, 0.02, 0.05, 0.1, and 1/3)

Anna Domgans,*,‡ Tobias Braun,‡ Davis Thomas Daniel, Nabi Aghdassi, Sebastian Speer, Andre Rossberg, Sebastian Schumacher, Evgeny V. Alekseev, Luc Raijmakers, Anna Windmüller, and Rüdiger-A. Eichel

Cite This: *ACS Appl. Energy Mater.* 2026, 9, 13655−13667

Read Online

ACCESS | Metrics & More | Article Recommendations | Supporting Information

ABSTRACT: P2-type layered oxides, particularly those based on Mn/Fe/Ni, are promising cathode materials for sodium-ion batteries but have structural instability caused by phase transitions during sodiation/desodiation. We show that the phase behavior of the P2-type material $Na_{0.66}Mn_{2/3}Fe_{1/3-x}Ni_x$ series (x = 0, 0.02, 0.05, and 1/3) is strongly influenced by the Fe/Mn/Ni cationic ratio, which is directly coupled to the Mn^{3+}/Mn^{4+} ratio. Powder X-ray diffraction reveals a systematic variation in the lattice parameter as a function of cation distribution, reflecting the corresponding changes in cation radii. Furthermore, the two binary systems exhibit different structural behaviors, with the Ni/Mn system forming a superstructure, whereas the Fe/Mn system does not exhibit such a phenomenon. The progressive narrowing of the linewidth determined by electron paramagnetic resonance indicates that the proportion of Mn^{3+} cations decreases as Ni^{2+} substitution in the P2 lattice increases. *In situ* XRD between 1.5 and 4.2 V vs Na/Na^+ shows that, in the absence or at low amounts of Ni^{2+} ($x < 0.05$), the P2 phase coexists with an undesired, Jahn–Teller-distorted orthorhombic P′2 phase. Notably, no high-voltage structural transformations to O2 or OP4/Z phases are observed above 4.0 V. At $x \geq 0.05$, the Mn^{3+} fraction is sufficiently reduced to suppress the formation of the P′2 phase in the low-voltage regime during discharge. These findings underscore the structural stabilization of Fe/Mn-based P2-type layered oxides achieved through minimal Ni substitution.

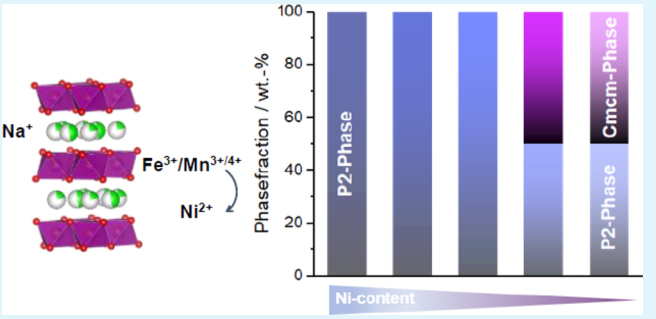

KEYWORDS: *sodium-ion batteries, Mn/Fe/Ni-based layered transition metal oxides, Jahn–Teller distortion, Raman spectroscopy, FTIR spectroscopy, in situ X-ray diffraction*

1. INTRODUCTION

Sodium-ion batteries (SIBs) have garnered significant attention due to their potential to offer a more sustainable alternative to lithium-ion batteries (LIBs). The abundance and nontoxic nature of Na in comparison to Li render SIBs an attractive side-by-side technology.[1−3] Their application is particularly advantageous for large grid systems, as they facilitate the storage of intermittent renewable energy and enhance its efficiency. Lately, SIBs have also been considered for low-cost electric vehicles as well as backup power systems.[2,4,5] SIBs and LIBs are based on similar working principles; however, there are discrepancies in the material development requirements for the anode and cathode given that Na (0.98 Å) has a larger ionic radius compared to Li (0.69 Å). Conversely, the molar mass of Na (23 g/mol) is greater than that of Li (6.9 g/mol), while the standard reduction potential of Na (−2.71 V vs SHE) is lower than that of Li (−3.06 V vs SHE). These factors contribute to a greater volume expansion during the charging and discharging processes and result in a reduction in specific capacity as well as lower transport kinetics and cycle life.[2,5,6]

Among the cathode material categories, layered transition metal oxides (LTMOs) Na_xTMO_2 (TM: transition metal) are a promising material class due to the high achievable specific capacity, ease of synthesis, and low costs.[7−9] Na-based LTMOs can be divided into the P2- and O3-type according to the Delmas notation.[10] The letters P and O stand for the Na-ion environment (prismatic and octahedral), and the numbers 2 and 3 stand for the stacking order of the layers. The formation of these specific polytypes is mainly governed by the initial sodium stoichiometry. While a higher sodium content typically stabilizes the O3 phase, a sodium content of around $x \leq 0.7$ generally favors the P2 structure.[10] Moreover, the structural properties are highly influenced by the ionic radii, valence

Received: August 5, 2026
Revised: September 30, 2026
Accepted: September 30, 2026
Published: October 8, 2026

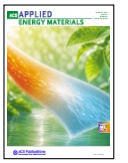

Downloaded from pubs.acs.org/aaemcq/article-pdf/9/20/13655/6878184/ae-2026-02501p.pdf by RWTH AACHEN HOCHSCHUL BIBL user on 10 November 2026

states, and specific ratios of the transition metals. Consequently, elemental substitution or slight variations in the transition metal framework can significantly shift the phase boundaries within the phase diagram, making the structural evolution highly sensitive to both the choice of dopants and their specific concentrations. Figure 1a illustrates three distinct single-component systems based on the TMs Ni, Mn, and Fe assuming the sodium content to be $x = 1$. While the Fe-based system ($NaFeO_2$) crystallizes in the ideal O3-type structure with space group $R\bar{3}m$,[11] in the Mn ($NaMnO_2$)–[12] and Ni ($NaNiO_2$)[13]-based systems, monoclinically distorted O3 structures are formed. These O′3 phases with space group $C2/m$ appear as a result of the Jahn–Teller distortion caused by the Jahn–Teller active Mn^{3+} and Ni^{3+} ions. Understanding this phase competition as a result of the sodium stoichiometry as well as the influences of the dopants is crucial for designing stable cathode materials, as it directly dictates not only the initial crystal structure but also the structural integrity during the subsequent electrochemical cycling, as the two polytypes exhibit phase transitions during sodiation/desodiation within the high-voltage range (>4.2 V) in the form of TM–O slab gliding, resulting in a substantial loss of capacity.[14] Even though the O3 types often offer higher initial capacities due to their higher initial Na content, they exhibit more complex phase transitions, changing from O3 → P3 → P3-O1, while P2 exhibits fewer phase transitions, changing from P2 → P2-O2. Consequently, the P2 type demonstrates superior capacity retention, more structural stability, and enhanced ionic conductivity, thereby broadening its application potential and making it more attractive compared to the O3 type.[15−17] Besides the high-voltage phase transition structural distortion also plays a role in the cathode materials as the ionization of TMs may be changed toward Jahn–Teller active ions during discharge.

Some of the most studied LTMOs are Ni/Mn-based LTMOs, which are characterized by the high-voltage $Ni^{2+}/Ni^{3+}/Ni^{4+}$ redox pair, which enables reversible capacities of around 140 mAh g^{-1} and a capacity retention of around 85% after 100 cycles at 0.05 C.[18,19] Fe/Mn-based systems, on the other hand, are promising as they benefit from low-cost, abundant raw materials and achieve specific capacities of over 190 mAh g^{-1} in the voltage range of 1.5–4.3 V.[18,20] However, both binary P2 cathode materials show a P2 to O2 phase transition at high charge potential (charge above 4.2 V vs Na/Na^+), which leads to a significant capacity loss. A further obstacle appears at potentials below 2 V vs Na/Na^+, as the Mn^{4+} ions are reduced to Mn^{3+} ions in high spin, with one electron remaining in the e_g orbital. The resulting elimination of the e_g degeneracy triggers a Jahn–Teller distortion of the MnO_6 octahedron and leads to the formation of the orthorhombic P′2 phase (space group $Cmcm$).[21] In addition, the Na^+/vacancy ordering in the P2-type binary Ni/Mn system leads to a honeycomb superstructure of Ni/Mn that significantly hinders Na diffusion, resulting in increased diffusion barriers and characteristic plateaus and voltage steps in the electrochemical profile.[1,22−25] This structural order arises because the Fermi levels of Ni and Mn are close to each other, a phenomenon not observed with other Fe/Mn analogs.[1] In addition, the use of Ni as a TM cathode material raises environmental and health concerns, as Ni compounds are toxic to humans and can leach into and contaminate soils, resulting in contamination. Moreover, Ni is not readily available, which makes it susceptible to process increases.[18]

Element substitution is an effective strategy for suppressing both the P2 to O2 phase transition and the Na^+/vacancy orders in the binary P2-type systems Fe/Mn and Ni/Mn. Both, "redox inactive" ions such as Li^+ or Mg^{2+} and "redox active" transition metals (e.g. Fe^{3+} and Ti^{4+}, Al^{3+}) can be used to modify the lattice dynamics and charge transport behavior.[26] For example, Ti substitution in the P2-$Na_{2/3}Ni_{1/3}Mn_{2/3-x}Ti_xO_2$ series showed that at $x = 1/6$ the characteristic voltage plateaus/steps completely disappear due to a realignment of the Na^+/vacancies, while at $x = 1/3$ the P2 to O2 transition is completely suppressed.[1,21] The elimination of Jahn-Teller distortions also prevents the formation of the P′2 modification and stabilizes the two-dimensional Na layer structure. In a further study, electrochemically active Fe^{3+} was introduced into the lattice to obtain $Na_{1/3}Ni_{1/3}Mn_{2/3-x}Fe_xO_2$ ($x = 0$, 1/24, 1/12, 1/8, and 1/6).[27] It could be shown that with increasing Fe content, the P2 structure becomes more resistant to phase transitions, and the charge–discharge profiles are significantly smoothed. Furthermore, doping with Li^+ or Mg^{2+} leads to a significant improvement in the cycle stability of Ni/Mn-based systems. For example, $Na_{2/3}Li_{0.1}Ni_{0.23}Mn_{0.67}O_2$ and $Na_{2/3}Mg_{0.1}Ni_{0.23}Mn_{0.67}O_2$ achieve specific capacities of 121.5 and 114.6 mAh g^{-1}, with the Mg-doped sample retaining 89.7% of its initial capacity after 100 cycles.[4]

While most studies investigate dopants like Fe at relatively low percentages, keeping the Ni content high, this work explores the critical lower limits of the Ni content in a ternary

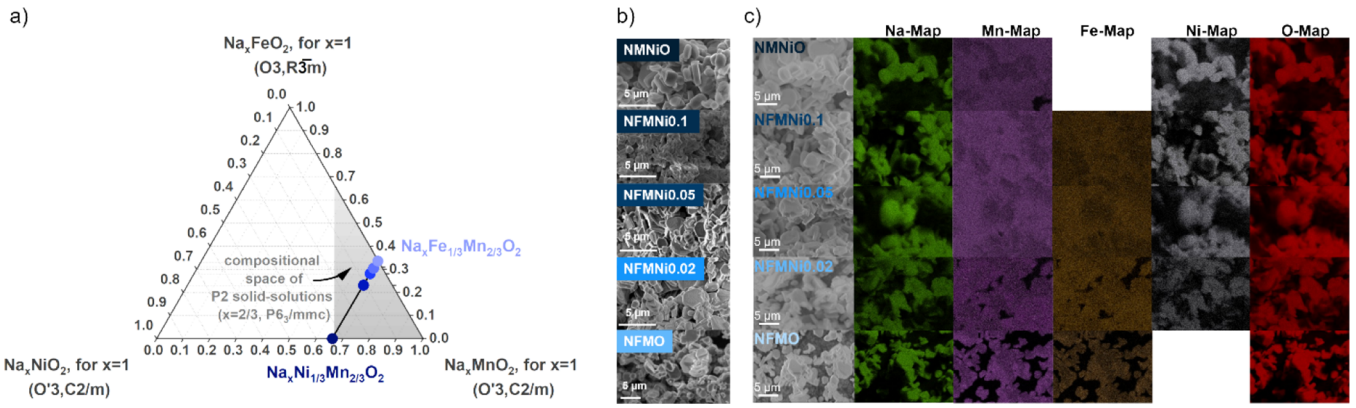

Figure 1. Ternary phase diagram of the P2-$Na_{0.66}Mn_{2/3}Fe_{1/3-x}Ni_x$ series ($x = 0$, 0.02, 0.05, 0.1, and 1/3) (a). SEM images of P2-$Na_{0.66}Mn_{2/3}Fe_{1/3-x}Ni_x$ ($x = 0$, 0.02, 0.05, 0.1, and 1/3) (b) and EDX mappings (c).

Downloaded from pubs.acs.org/aaemcq/article-pdf/9/20/13655/6878184/ae-2026-02501p.pdf by RWTH AACHEN HOCHSCHUL BIBL user on 10 November 2026

https://doi.org/10.1021/acsaem.6c02501
ACS Appl. Energy Mater. 2026, 9, 13655−13667

system by investigating the P2-$Na_{0.66}Mn_{2/3}Fe_{1/3-x}Ni_x$ series (x = 0, 0.02, 0.05, and 1/3). By systematically tuning the Mn/Fe/Ni ratio, we aim to determine the optimal synergy between the three transition metals, searching for the lowest Ni content to suppress Jahn–Teller distortions. This approach addresses the gap of how to improve structural and electrochemical performance while strictly minimizing the content of the toxic Ni. Comprehensive phase and structural analysis is performed using powder X-ray diffraction (PXRD), *in situ* X-ray diffraction, extended X-ray absorption fine structure (EXAFS), Fourier-transform infrared spectroscopy (FTIR), and Raman and electron paramagnetic resonance (EPR) spectroscopy. Finally, the electrochemical behavior of each composition is evaluated by cyclic voltammetry and galvanostatic cycling to correlate atomic-level modifications with battery-relevant properties.

2. EXPERIMENTAL SECTION

2.1. Synthesis

P2-$Na_{2/3}Mn_{2/3}Ni_{1/3}O_2$ (NMNiO), P2-$Na_{2/3}Mn_{2/3}Fe_{0.23}Ni_{0.1}O_2$ (NFMNi0.1), P2-$Na_{2/3}Mn_{2/3}Fe_{0.28}Ni_{0.05}O_2$ (NFMNi0.05), P2-$Na_{2/3}Mn_{2/3}Fe_{0.31}Ni_{0.02}O_2$ (NFMNi0.02), and P2-$Na_{2/3}Mn_{2/3}Fe_{1/3}O_2$ (NFMO) were synthesized by a two-step solid-state reaction, as previously reported.[28] The precursors Na_2CO_3 decahydrate, Fe_2O_3, MnO_2, and NiO were mixed in the motar grinder (Retsch RM 200). The mixed powder was transferred into a crucible and calcined in air at 600 °C for 8 h. The calcined powder was mixed again and then pressed into a pellet and sintered in air at 900 °C for 12 h. The pellet was cooled to room temperature, ground in a mortar, and immediately transferred to an argon-filled glove box to protect the powder from moisture. The cation stoichiometry was determined using inductively coupled plasma optical emission spectrometry (ICP-OES) (Table S1).

2.2. Scanning Electron Microscopy and Energy-Dispersive X-ray Spectroscopy

SEM images were obtained using a Quanta FEG 650 FEI (USA). The samples were first placed in a Kammrath & Weiss transfer vessel in a glove box to protect them from exposure to ambient air. The images were recorded using an e-beam accelerator with an acceleration voltage of 5/10 kV and a secondary electron detector. The chemical distribution was determined using an integrated energy-dispersive spectrometer (EDS) (Ametek, USA).

2.3. Powder X-ray Diffraction

PXRD patterns were recorded by a lab diffractometer (Empyrean, Panalytical) with a copper anode at a Kα wavelength of 1.5406 Å. The powders were prepared in a back-load sample holder. The measurements were recorded in a Bragg–Brentano geometry in a 2θ range 10–100° with a step size of 0.0072°. Quantitative phase analysis (QPA) based on PXRD data was performed using the Diffrac.Topas Version 7 software package (Bruker). Crystal size, strain, and lattice parameters were determined using the Pawley method. In Rietveld refinement analyses, the occupancy factors, thermal Debye–Waller factors, and scaling factors were refined.

In situ XRD patterns were recorded by a lab diffractometer (Empyrean, Panalytical) with a silver anode at a Kα wavelength of 0.5594 Å. The measurements were recorded in a self-made *in situ* coin cell with aluminum windows in a Debye–Scherrer geometry in a 2θ range 3–30°. The lattice parameters and volume of *in situ* measurements were determined using the Diffrac.Topas Version 7 software package (Bruker).

For the fitting of the *in situ* XRD patterns, the refined parameters of all five samples from the Rietveld refinement of the PXRD data were used as initial values for the lattice parameters. The Al/Na reflection peak profiles were adjusted in the first scans to account for preferred orientation and size effects and were subsequently fixed for all subsequent scans. Strains, occupancies, and thermal Debye–Waller factors were kept constant. Only the lattice parameters a_{hex} and c_{hex}, as well as the size of the P2 structure, were refined to track a/c over multiple scans. To follow the evolution of the P′2 phase (*Cmcm*), the structure of $Na_{0.96}Fe_{1/3}Mn_2/3O_2$ (ICSD code 231008[29]) was used as a reference.

For the quantification of the *in situ* XRD patterns, first the structural parameters of the P′2 (*Cmcm*) phase was determined from the last scan showing a clear presence of this phase. Then the blank value was determined from the first scan, where no P′2 phase is expected. For each individual scan, the P′2 model was applied using the parameters determined from the previous scan. The lattice parameters (a/c and size and strain) were fixed, while the relevant intensity/scalefactor was freely adjusted. Exceeding the blank value indicates the onset of significant P′2 formation. For scans below the transition, only the P2 phase was included in the fit, as the P′2 contribution is below the significance threshold. Starting from the scan in which *Cmcm* becomes significant, P2 and P′2 were fitted simultaneously. The lattice parameters and scale factors are refined, while all other structural parameters were kept fixed. The relative phase fractions were then calculated from the resulting quantitative phase fractions.

2.4. Extended X-ray Absorption Fine Structure

Mn K-edge (6539 eV), Fe K-edge (7112 eV), and Ni K-edge (8333 eV) X-ray absorption spectra of P2-$Na_{0.66}Mn_{2/3}Fe_{1/3}O_2$ and $Na_{0.66}Mn_{2/3}Ni_{1/3}O_2$ were collected at the Rossendorf Beamline (ROBL, BM20) at the European Synchrotron Radiation Facility (ESRF),[30] operated at an electron energy of 6 GeV and a beam current of 200 mA. The incident white X-ray beam was monochromatized using a liquid-nitrogen-cooled Si(111) double-crystal monochromator in channel-cut mode, and higher-order harmonics were suppressed by two Rh-coated mirrors. All spectra were acquired in fluorescence mode, with the fluorescence signal detected by an 18-element, high-throughput Ge detector (Mirion). The incident photon flux and the absorption of the sample and the metal reference foils were monitored using gas-filled ionization chambers.

Samples were prepared by homogeneously mixing the respective cathode materials with predried boron nitride (BN; 700 °C, 100 h) as a diluent to achieve an appropriate absorption length. The resulting powder mixtures were spread uniformly onto EXAFS sample holders and sealed with Kapton tape. All samples were measured under cryogenic conditions at 15 K using a closed-cycle He cryostat to minimize thermal disorder and to prevent radiation-induced sample damage during data collection. For each sample, multiple energy scans were accumulated and subsequently averaged to achieve a sufficient signal-to-noise ratio. Energy calibration was performed by simultaneously recording the absorption spectrum of the respective metal reference foil (Mn, Fe, or Ni) during each scan, with the first inflection point of the K-edge of each foil serving as the energy reference.

Data reduction, including dead-time correction, statistical weighting of the individual fluorescence detector channels, energy calibration, averaging of multiple scans, and EXAFS signal extraction, was performed using Larch. Subsequent shell fits were carried out in R-space, employing theoretical scattering phase and amplitude functions calculated with the *ab initio* real-space multiple-scattering code FEFF 8.2027.[31] These calculations relied on structural models derived from the known crystal structures of P2-$Na_{0.66}Mn_{2/3}Fe_{1/3}O_2$ (ICSD code 231006) and $Na_{0.66}Mn_{2/3}Ni_{1/3}O_2$ (ICSD code 33347). During the fitting procedure, the coordination numbers (N) were constrained to their theoretical crystallographic values, and a single global energy shift (ΔE_0) was applied to all scattering paths within the same absorption edge. Meanwhile, the changes in half-path length (ΔR) and the Debye–Waller factors (σ^2) were treated as independent floating parameters during the fitting procedure.

Downloaded from pubs.acs.org/aaemcq/article-pdf/9/20/13655/6878184/ae-2026-02501p.pdf by RWTH AACHEN HOCHSCHUL BIBL user on 10 November 2026

https://doi.org/10.1021/acsaem.6c02501
ACS Appl. Energy Mater. 2026, 9, 13655−13667

2.5. Raman Spectroscopy

Raman spectroscopy on the P2-$Na_{0.66}Mn_{2/3}Fe_{1/3-x}Ni_xO_2$ series (x = 0, 0.02, 0.05, 0.1, and 1/3) was conducted with a WITEC alpha300R microscope using a solid-state 532 nm excitation laser. The spectra were recorded by using a 600 l/mm grating and 0.1 mW laser power. An area of 50 × 50 μm was mapped on each sample with a 50× objective and a step size of 1 μm. The recorded spectra were evaluated by a correction algorithm for cosmic ray removal and baseline correction. The processed spectra of the P2-$Na_{0.66}Mn_{2/3}Fe_{1/3-x}Ni_x$ series (x = 0, 0.02, 0.05, 0.1, and 1/3) were fitted using pseudo-Voigt function starting with literature band positions of NFMO (E_{1g} + $3E_{2g}$ + A_{1g} with 166, 367, 459, 581, and 619 cm^{-1}).[32]

2.6. Fourier-Transform Infrared Spectroscopy

To carry out FTIR measurements, the samples were mixed with KBr powder and pressed into pellets, each with a diameter of 11 mm. Spectra were recorded with a Bruker spectrometer (model Vertex 80v) in transmission mode on all sample pellets with the beam path fully evacuated ($p \leq 2.4$ mbar). A background recorded beforehand on an empty pellet holder was subtracted from the raw data obtained for each sample.

2.7. Electron Paramagnetic Resonance Spectroscopy

EPR spectroscopic measurements were done using powder samples of P2-$Na_{0.66}Mn_{2/3}Fe_{1/3-x}Ni_xO_2$ series (x = 0, 0.02, 0.05, 0.1, and 1/3) that were filled into 4 mm (outer diameter) EPR tubes. The spectra were recorded at room temperature with a Bruker EMXnano EPR spectrometer operating at a frequency of 9.4 GHz (X-band). Spectra were acquired with a modulation amplitude of 0.1 mT and a modulation frequency of 100 KHz with a microwave power of 1.5 mW.

2.8. Electrochemical Measurement

The electrodes for each material were prepared by mixing the active material with polyvinyldene fluoride (PVDF) as a binder and carbon black (Super P) in a ratio of 70:15:15 in *N*-methly-2-pyrrolidone (NMP) as a solvent. The resulting slurry was applied to an Al foil using a doctor blade. After drying at 120 °C for 1 h on the heating plate, cathodes with a diameter of 11 mm were punched out of the sheets containing an active material loading of 2–3 mg/cm^2. These were then dried overnight in a high vacuum. All electrochemical experiments were carried out in half-cells (Swagelok cells), with the cathode being tested against a sodium metal counter electrode. The separator stack consisted of two Celgard 2500 membranes in combination with one glass fiber (Whatman GF/D) in between. The electrolyte consisted of a mixture of 0.9 M $NaPF_6$ (Sigma-Aldrich, 98%) and 0.1 M $NaBF_4$ (Sigma-Aldrich, 98%) in diethylene glycol-dimethyl ether (Sigma-Aldrich, anhydrous 99.5%). An amount of 200 and 150 μL electrolyte was used in the Swagelok cells and *in situ* cells, respectively. All measurements were carried out using a Biologic MPG-200 potentiostat, with the cells stored at 25 °C in a climate chamber. Cyclic voltammetry (CV) experiments ($n \geq 3$) were carried out within a potential window of 1.5–4 and 1.5–4.2 V vs Na/Na^+ with a scanning rate of 0.02 mV s^{-1}. Galvanostatic charge/discharge measurements ($n \geq 3$) were carried out with at 0.05 C in a potential range of 1.5–4.2 V vs Na/Na^+. Specific capacities were calculated based on the active material loading of the electrodes. Theoretical capacities were derived from the molar mass of the respective material compositions according to Faraday's law. The galvanostatic charge/discharge profiles were later normalized to the initial discharge capacity. Galvanostatic charge/discharge measurements of the *in situ* XRD measurements were also performed with a Biologic Model MPG-200 potentiostat. The first cycle was measured within the potential window of 1.5 and 4.2 V vs Na/Na^+.

3. RESULTS AND DISCUSSION

3.1. Microstructure

The P2-$Na_{2/3}Mn_{2/3}Fe_{1/3-x}Ni_x$ (x = 0, 0.02, 0.05, 0.1, and 1/3) (NFMO, NFMNi0.02, NFMNi0.05, NFMNi0.1, an NMNiO) series was produced via a two-step solid-state synthesis, with all compositions expected to form a solid solution with a hexagonal P2-type layered oxide structure (Figure 1a). As revealed by SEM analysis, all five samples consist of fine-grained powders with irregular shapes of the particles (Figure 1b). As expected, the primary particles have a platelet-like morphology for the P2-type structure with an average particle size of 2 μm. EDX analysis with corresponding elemental mapping shows a uniform distribution of the elements according to their respective compositions, with no detectable agglomerates or secondary phases (Figure 1c). The Ni signal continuously decreases, while the Fe signal increases, from NMNiO to NFMO, suggesting the successful synthesis of the P2-$Na_{2/3}Mn_{2/3}Fe_{1/3-x}Ni_x$ (x = 0, 0.02, 0.05, 0.1, and 1/3) series. To further verify the crystal structure of the different compounds, quantitative phase analysis (QPA) based on PXRD measurements was conducted.

For the QPA and Rietveld refinement analysis based on PXRD measurements of the P2-$Na_{2/3}Mn_{2/3}Fe_{1/3-x}Ni_x$ (x = 0, 0.02, 0.05, 0.1, 1/3) series, P2-NMNiO (ICSD code 33347) and P2-NFMO (ICSD code 231006) structures with a hexagonal $P6_3/mmc$ space group were used as a starting model for the fit. The lattice parameter, size, and strain were determined using the Pawley method.[33] For the Rietveld refinement analysis, the scale factor, thermal Debye–Waller factors, and occupancies were refined. Figure 2a,b and Figure S1 in the Supporting Information show the analysis results from all five samples.

The analysis for NMNiO reveals a fraction of 98.26 wt % of the P2-NMNiO main phase and a small proportion of 1.74 wt % NiO as a secondary phase. This secondary phase arises from the limited solubility within the P2 phase.[34] Nevertheless, ICP-OES analysis confirms the targeted bulk stoichiometry of NMNiO and the other samples (Table S1 in the Supporting Information), albeit with variations in the Na content. The lattice parameters of the P2 main phase of NMNiO were determined to be a_{hex} = 2.89054(5) Å and c_{hex} = 11.1484(5) Å, corresponding to a unit cell volume of 80.668(4) $Å^3$, in good agreement with literature values.[6,18,21,35] The two additional peaks appearing at 27.19° and 28.35°, which cannot be described by the fit model, indicate a coupled structural order (Figure 2c) as reported in the literature.[4,18,23,25] The structural ordering leads to a honeycomb arrangement of the TMs Ni and Mn in NMNiO, which correlates with a zigzag-type Na^+/vacancy ordering (Figure 2d).

The analysis of the four additional samples, NFMNi0.1, NFMNi0.05, NFMNi0.02, and NFMO, yields a single-phase material without any impurity phases. The lattice parameters and volume of the unit cell determined from the Rietveld refinement analysis increase linearly with the Fe content from a_{hex} = 2.90947(3) Å, c_{hex} = 11.1877(3) Å, and 82.016(3) $Å^3$ for NFMNi0.1 to a_{hex} = 2.91167(4) Å, c_{hex} = 11.1975(4) Å, and 82.212(4) $Å^3$ for NFMNi0.05 to a_{hex} = 2.91384(4) Å, c_{hex} = 11.2194(3) Å, and 82.495(3) $Å^3$ for NFMNi0.02 and finally to a_{hex} = 2.91898(4) Å, c_{hex} = 11.2368(4) Å, and 82.916(4) $Å^3$ for NFMO (Figure 2e and Table S2). The determined values for NFMO agree well with the previously reported values.[20,21,29,36]

Downloaded from pubs.acs.org/aaemcq/article-pdf/9/20/13655/6878184/8/ae-2026-02501p.pdf by RWTH AACHEN HOCHSCHUL BIBL user on 10 November 2026

https://doi.org/10.1021/acsaem.6c02501
ACS Appl. Energy Mater. 2026, 9, 13655−13667

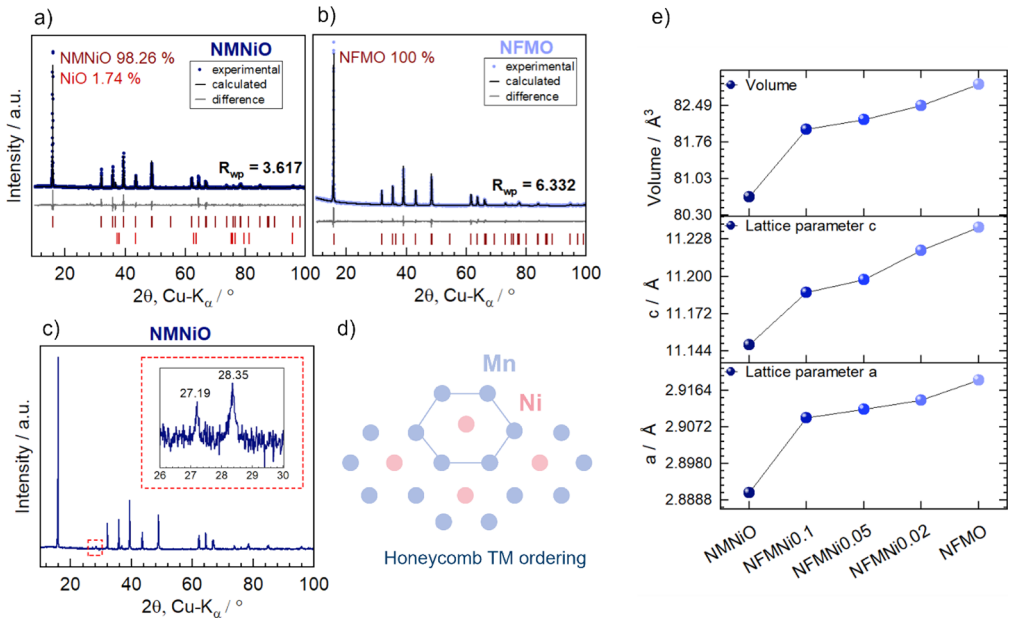

Figure 2. Rietveld refinement of PXRD measurements of P2-$Na_{0.66}Mn_{2/3}Fe_{1/3-x}Ni_x$ ($x = 0$ and 1/3) (a, b). PXRD of NMNiO. Enlarged superstructure of NMNiO (c). Schematic illustration of the honeycomb ordering of Ni/Mn metals (d). Lattice parameters a_{hex}/c_{hex} and volume of P2-$Na_{0.66}Mn_{2/3}Fe_{1/3-x}Ni_x$ ($x = 0$, 0.02, 0.05, 0.1, and 1/3) (e).

The increase in the lattice parameters a_{hex} and c_{hex}, as well as in the unit cell volume, correlates with increasing Fe content due to changes in the Mn^{3+}/Mn^{4+} ratio in the different compounds, although the calculated Mn^{3+}/Mn^{4+} ratio of ICP-OES results suggests a nonmonotonic trend (Supporting Information, Table S1). Mn and Ni in NMNiO are present in the oxidation states +4 and +2. Charge imbalance caused by the substitution of Ni^{2+} with Fe^{3+} partially is compensated by the partial reduction of Mn^{4+} species to Mn^{3+}. The larger radius of Mn^{3+} (0.645 Å, VI) compared to Mn^{4+} (0.53 Å, VI) causes the expansion of lattice parameter and volume. Moreover, the variation in Na content, as confirmed by the ICP-OES results, does not appear to have a significant influence on the lattice parameter. An increase in Na content would generally be expected to increase the a_{hex} lattice parameter. However, despite the increase in Na content from NFMO (Na: 0.68 ± 0.0011) to NFMNi0.02 (Na: 0.73 ± 0.0010), the lattice parameter increases monotonically across the investigated samples.

A detailed overview of the valence states and their assumed corresponding fractions in the respective components is presented in Table 1.[24,29]

QPA based on PXRD confirmed the successful synthesis of the P2-$Na_{2/3}Mn_{2/3}Fe_{1/3-x}Ni_x$ ($x = 0$, 0.02, 0.05, 0.1, 1/3) series and shows the influence of the TM Ni/Mn/Fe ratio on the lattice parameter.

Table 1. Nominal Charge-Balance Model for the Formal Oxidation States of P2-$Na_{0.66}Mn_{2/3}Fe_{1/3-x}Ni_x$ ($x = 0$, 0.02, 0.05, 0.1, and 1/3)

sample	valence states
NMNiO	$Na^{+I}_{2/3}Mn^{+IV}_{2/3}Ni^{+II}_{1/3}O^{-II}_{2}$
NFMNi0.1	$Na^{+I}_{2/3}Fe^{+III}_{0.23}Mn^{+III}_{0.23}Mn^{+IV}_{0.44}Ni^{+II}_{0.1}O^{-II}_{2}$
NFMNi0.05	$Na^{+I}_{2/3}Fe^{+III}_{0.28}Mn^{+III}_{0.29}Mn^{+IV}_{0.38}Ni^{+II}_{0.05}O^{-II}_{2}$
NFMNi0.02	$Na^{+I}_{2/3}Fe^{+III}_{0.31}Mn^{+III}_{0.32}Mn^{+IV}_{0.35}Ni^{+II}_{0.02}O^{-II}_{2}$
NFMO	$Na^{+I}_{2/3}Fe^{+III}_{1/3}Mn^{+III}_{0.33}Mn^{+IV}_{0.34}O^{-II}_{2}$

To verify interatomic distances and investigate the formation of the TM ordering superstructure, EXAFS measurements were conducted on NFMO and NMNiO. Figure 3a,b shows Fourier-transformed spectra at the Mn/Fe K-edge for NFMO and at the Mn/Ni K-edge for NMNiO. Two distinct peaks can be observed in all spectra of the Mn/Fe/Ni K edge, which can be attributed to the nearest oxygen and TM-Na neighbors. The peaks are similar in shape, indicating a homogeneous distribution of Mn/Fe/Ni in the material.[37] In addition, three less intense peaks are visible, which can be assigned to the next shells and thus to the next-neighbors TM-Fe/Ni/Na/O.

It is also notable that the Mn K-edge spectra of both materials exhibit lower intensities than the corresponding Fe and Ni K-edge spectra. This can be explained by the specific structural characteristics of the two materials. In NFMO, Mn exists in a mixed valence state between Mn^{3+} and Mn^{4+}. The Jahn–Teller distortion of the high-spin Mn^{3+} introduces distinct short and long Mn–O bonds, which broaden the overall radial distribution of the first coordination shell and dampen the EXAFS signal. In NMNiO, on the other hand, the lattice exhibits a higher structural order in the form of a honeycomb superstructure, in which the Mn atoms are arranged hexagonally around a Ni atom (Figure 2d). As already evidenced by the additional reflections in the PXRD spectrum in Figure 2c, it stands to reason that Mn therefore has different bond lengths to their surrounding oxygen atoms, which in turn results in a reduced intensity of the corresponding peak in the spectrum.[4,18,23,25] In addition to peak intensity, the coordination numbers of the Mn–O bonds also reflect inhomogeneity in the Mn environment. NFMO exhibits a lower coordination number (2.0) than NMNiO (2.4), which supports the claim that these are two different structural mechanisms. A comparison of the distances obtained from the fitting (Table S3 in the Supporting Information) shows that the Mn–O bond lengths for NFMO (1.905(6) Å) and

Downloaded from pubs.acs.org/aaemcq/article-pdf/9/20/13655/6878184/aae-2026-02501p.pdf by RWTH AACHEN HOCHSCHUL BIBL user on 10 November 2026

https://doi.org/10.1021/acsaem.6c02501
ACS Appl. Energy Mater. 2026, 9, 13655−13667

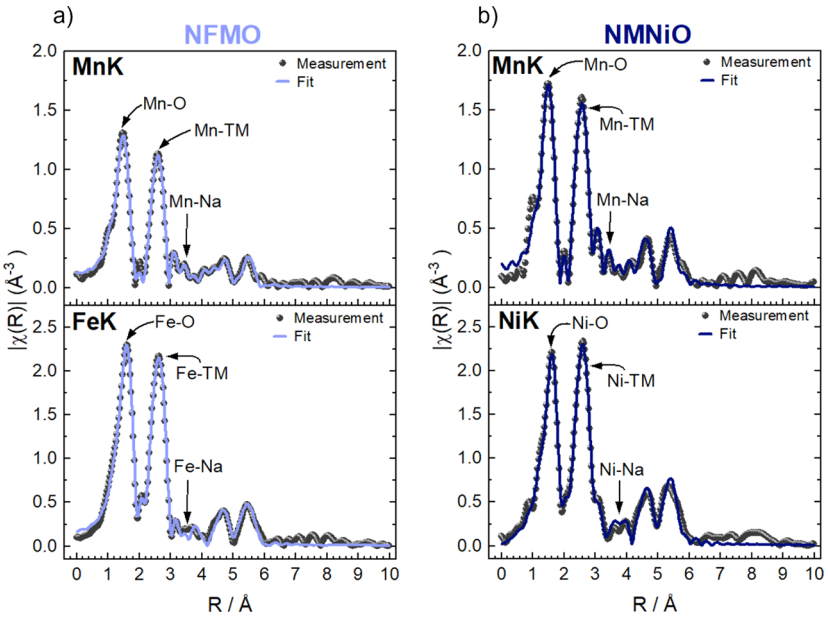

Figure 3. EXAFS measurements of the Mn/Fe K-edge from NFMO (a) and the Mn/Ni K-edge from NMNiO (b).

NMNiO (1.904(5) Å) are practically identical, while a slightly larger deviation is observed for the Mn–Na distances (3.10(2) vs 3.06(2) Å). For the Fe–O coordination in NFMO, a bond distance of 2.011(5) Å is obtained, which shows that Fe behaves differently from Mn even though both occupy the same positions. The longer Fe–O distances compared to the Mn–O bond length (1.905(6) Å) are consistent with the lager ionic radius of high-spin Fe^{3+} relative to Mn^{4+}. Moreover, unlike Mn^{3+} ions, high-spin Fe^{3+} ions do not undergo Jahn–Teller distortion, which lead to a more symmetric and distinct local coordination environment, reflected in different bond lengths. Furthermore, the Ni–O distance in NMNiO is slightly longer at 2.042(6) Å. The same trend is observed for the Fe–Na and Ni–Na shells, with distances of 2.84(7) and 2.99(8) Å, respectively. This is consistent with the larger ionic radius of Ni^{2+} compared to Fe^{3+}.

The PXRD analyses show a decrease in the lattice parameters a_{hex} and c_{hex} with increasing Ni content. This can be attributed to the fact that NFMO contains a mixture of 0.33 Mn^{3+} and 0.34 Mn^{4+}. When Fe is completely substituted by Ni (NMNiO), the proportion of Mn^{4+} increases to 0.67 to balance the charge in the material. Since the ion radius of Mn^{4+} is smaller than that of Mn^{3+}, the decreasing trend in lattice parameters is expected and leads to the initial assumption that the distances from EXAFS measurements must also be smaller for NMNiO than for NFMO. This expectation is indeed consistent with the results for the Mn K-edge, where NMNiO exhibits smaller distances overall than NFMO. This can be attributed to the substitution of Fe with Ni, which leads to a higher Mn^{4+} content and, consequently, to smaller average Mn–O distances due to the smaller ionic radius of Mn^{4+}. In contrast, the distances determined at the Ni K-edge region are larger than those observed at the Fe K-edge region, which may be related to the differences in the ionic radii of Ni and Fe. However, the differences between the PXRD and EXAFS results can be explained by the different aspects of the structure that the two methods investigate. While PXRD provides information about the average long-range crystal structure of the entire sample, EXAFS examines the local atomic environment around the absorbing atom. In NMNiO, the presence of a superstructure in which Mn atoms form hexagonal arrangements with Ni at their center can lead to local structural configurations that are not fully reflected in the average lattice parameters determined by PXRD. Consequently, larger local distances can be observed using EXAFS despite the general decrease in lattice parameters.

3.2. Spectroscopy Methods to Investigate the Influence of the Ni/Fe/Mn Ratio

Raman, FTIR, and EPR spectroscopy were used to probe changes in the local bonding environment as a function of Ni/Mn/Fe ratio (Figure 4a–c).

The Raman spectra for all components were fitted using the pseudo-Voigt function starting with the five literature-known band positions for NFMO at 166, 367, 459, 581, and 619 cm^{-1},[32] which can be assigned to the Raman modes $E_{1g} + 3E_{2g} + A_{1g}$ (Figure 4a). For NFMNi0.02-Ni0.1, the expected five modes are observed, whereas NMNiO exhibits an additional sixth mode ($E_{2g}(4)$). The determined band positions of the individual modes (Figure S2 in the Supporting Information) reveal a red shift for the A_{1g} and $E_{1g}(1/3)$ mode for NFMO and NFMNi0.02-0.1. The $E_{2g}(2)$ vibration behaves differently. In contrast, NMNiO shows a consistent red shift for all vibrational modes.

Given the higher electronegativity of Ni compared to Fe and the increased Mn^{4+} content with increasing Ni concentration, shorter and stronger TM–O bonds are expected, which would lead to a blue shift. However, for the ternary Fe/Mn/Ni compounds (NFMNi0.02-0.1), increasing disorder weakens the local bonding environment despite shorter bond lengths, leading to an overall red shift of the Raman active modes.[26,38] Moreover, NMNiO (Ni/Mn) forms a honeycomb-like arrangement of TM, and the accompanying Na^+ vacancies arrange into a layered LZZ (large zigzag) superstructure, which is confirmed by PXRD.[4,24,39,40] This highly ordered structure reduces local distortions, leading to the formation of an additional Raman mode ($E_{2g}(4)$) as well as softer TM–O vibrations, which cause

Downloaded from pubs.acs.org/aaemcq/article-pdf/9/20/13655/6878184/aae-2026-02501p.pdf by RWTH AACHEN HOCHSCHUL BIBL user on 10 November 2026

https://doi.org/10.1021/acsaem.6c02501
ACS Appl. Energy Mater. 2026, 9, 13655−13667

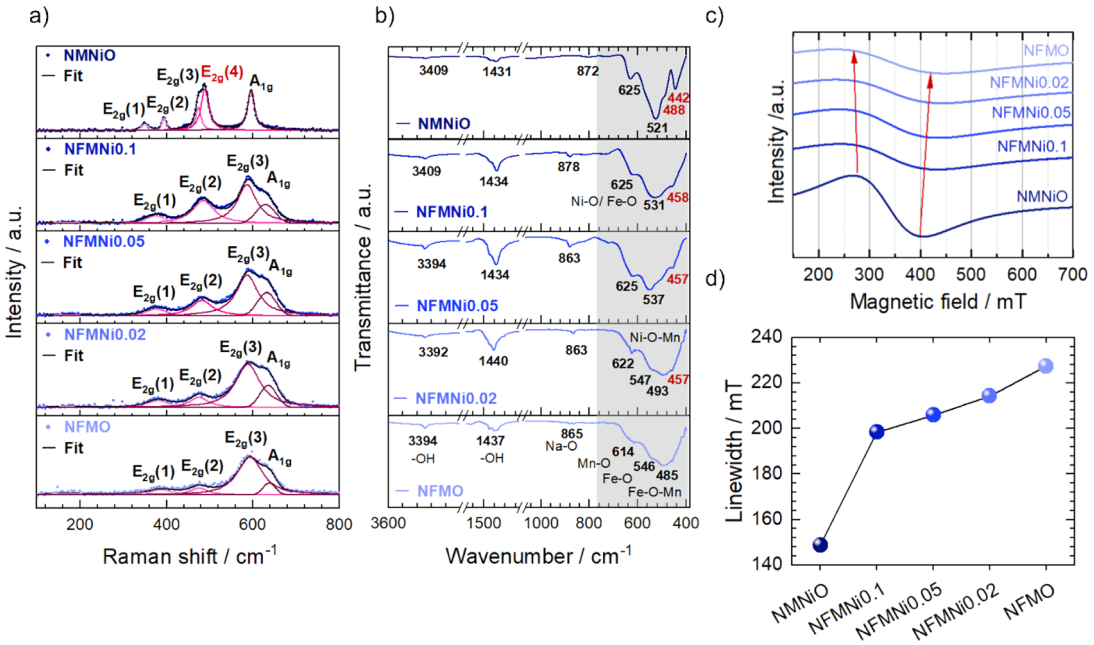

Figure 4. Fitted Raman measurements of P2-$Na_{0.66}Mn_{2/3}Fe_{1/3-x}Ni_x$ (x = 0, 0.02, 0.05, 0.1, and 1/3) (a). FTIR measurements of P2-$Na_{0.66}Mn_{2/3}Fe_{1/3-x}Ni_x$ (x = 0, 0.02, 0.05, 0.1, and 1/3) (b). X-band EPR measurements of P2-$Na_{0.66}Mn_{2/3}Fe_{1/3-x}Ni_x$ (x = 0, 0.02, 0.05, 0.1, and 1/3) (c). Peak-to-peak linewidth from EPR measurements (d).

further red shift. Furthermore, the vibration frequency ω is inversely proportional to the square root of the reduced mass μ and directly proportional to the square root of the force constant k. Since atomic mass increases in the order Mn < Fe < Ni, the reduced mass μ of the TM–O unit also increases with higher Ni content. This contributes to a lower vibration frequency ω, which further enhances the observed red shift. These results corroborate the EXAFS findings, which indicate longer bond lengths in NMNiO than in NFMO.

The apparent discrepancy between Raman and EXAFS on the one hand and PXRD on the other arises from the different structural information probed by the techniques. PXRD determines the average crystallographic bond length over the long range, while EXAFS probes the local coordination environment around individual atoms.

Figure 4b shows the FTIR spectra between 3600 and 400 cm^{-1}. The bands in the ranges of 3309–3409 and 1431–1440 cm^{-1} can be assigned to OH bending and OH stretching vibrations confirming the presence of NaOH and Na_2CO_3 on the particles, which occur as side products from the LTMO synthesis.[41] In the low-frequency region between 400 and 700 cm^{-1} (highlighted in gray in Figure 4b), the TM–O vibration modes are observed. With increasing Ni content, the bands between 620 and 485 cm^{-1} become narrow. In addition, new bands emerge in the low-frequency region (≈457 and 442 cm^{-1}), which can be attributed to Ni–O vibrations, confirming the incorporation of Ni into the lattice. The spectrum of NMNiO shows sharper bands, attributed to its highly ordered structure, in agreement with Raman and PXRD results that indicate superstructure formation and lattice changes upon variation of the Fe/Mn/Ni ratio.[42] Moreover, the FTIR results indicate the presence of NaOH, suggesting that variations in the Na content determined by ICP-OES may partly originate from differences in the residual NaOH/Na_2CO_3 content of the bulk material rather than from changes in the Mn^{3+}/Mn^{4+} ratio in the P2 material. Therefore, the apparent nonmonotonic variation of the Mn^{3+}/Mn^{4+} ratio inferred from the ICP-OES results alone may not reflect the actual Mn oxidation state. This interpretation is further supported by the PXRD results, which show a monotonic trend of the lattice parameter with increasing Ni substitution. Thus, considering the FTIR and PXRD results together, the data are consistent with a decrease in the Mn^{3+} fraction with increasing Ni^{2+} content. To complement these results, EPR spectroscopy was employed, revealing changes in the local coordination environment as a function of the Fe/Mn/Ni ratio (Figure 4c,d). EPR spectra of LTMOs is affected by exchange interactions usually leading to featureless spectra with large linewidths.[43] These interactions arise from spin exchange between neighboring metal ions and can occur as direct exchange, double exchange (between mixed-valence ions), or superexchange mediated by oxygen. The strength of these interactions is reflected in the EPR linewidth, with narrower lines corresponding to more efficient spin exchange. Therefore, the linewidth can be used as an indicator of change in the valence of the metal ions, their spatial proximity, and structural rearrangement. The narrowest peak-to-peak linewidth is observed for NMNiO (148.8 mT). With increasing Fe content, the linewidth increases steadily, reaching a maximum for NFMO (227.4 mT), corresponding to a difference of 78.6 mT.

The presence of an EPR signal in NMNiO, which does not contain Fe^{3+}, suggests that the observed signal originates predominantly from the Mn^{4+} species. Ni^{2+} (d^8, S = 1) and Mn^{3+} (d^4, S = 2) signals are typically not observed with X-band EPR at room temperature owing to rapid spin relaxation and broad resonance lines resulting from zero-field splitting.[44] Substitution of Ni^{2+} by Fe^{3+} requires charge compensation, leading to the formation of Mn^{3+} and an increased Mn^{3+}/Mn^{4+} ratio (Figure S3 in the Supporting Information and Table 1). The observed evolution of the EPR spectra in

https://doi.org/10.1021/acsaem.6c02501
ACS Appl. Energy Mater. 2026, 9, 13655−13667

Downloaded from pubs.acs.org/aaemcq/article-pdf/9/20/13655/6878184/aae-2026-02501p.pdf by RWTH AACHEN HOCHSCHUL BIBL user on 10 November 2026

the Ni/Fe/Mn system is primarily governed by changes in the Mn valence distribution. As a reference, the EPR spectrum of MnO_2 shown in Figure S4 exhibits a comparatively narrow linewidth (28.8 mT) due to superexchange interactions between Mn^{4+} ions mediated by oxygen. The presence of Ni^{2+} in NMNiO affects these exchange interactions and leads to a broadening of the signal in agreement with previous reports.[45] A complete substitution with Fe instead of Ni, as in the case of NFMO, leads to an even larger linewidth difference from MnO_2, suggesting that Fe substitution has a stronger influence on the line broadening. With increasing Fe content, the fraction of Mn^{3+} increases, promoting double-exchange interactions between Mn^{3+} and Mn^{4+}, which further broaden the EPR signal in comparison to NMNiO.[46] EPR analysis reveals that the coordination environment of Mn^{4+} evolves with increasing Fe content, indicating the successful tuning of the Fe/Mn/Ni ratio in the LTMO. This is consistent with the results of the Rietveld refinement, Raman spectroscopy, and FTIR spectroscopy, all of which confirm changes in the local environment as the system evolves from a binary (NFMO) to ternary composition (NFMNi0.02-0.1) and back to a highly ordered Ni/Mn binary phase (NMNiO). Furthermore, the EPR results provide further support for the assumption of a monotonic decrease in the Mn^{3+} proportion with increasing Ni^{2+} substitution despite the apparent nonmonotonic trend suggested by the ICP-OES results (Supporting Information, Table S1).

3.3. Electrochemistry

Electrochemical experiments were performed to evaluate the influence of the different cation ratios on the electrochemical performance (Figure 5a–c).

The CV measurements were recorded between 1.5 and 4.0 V and 1.5 and 4.2 V vs Na/Na^+ (Figure 5a,b). NMNiO exhibits three distinct oxidation peaks at 2.09, 3.22/3.38, and 3.67/3.73 V vs Na/Na^+, which can be assigned to the redox pairs Mn^{3+}/Mn^{4+}, Ni^{2+}/Ni^{3+}, and Ni^{3+}/Ni^{4+}, respectively.[47] The corresponding reduction peaks occur at lower potentials, i.e., at 1.73, 3.08/3.23, and 3.53/3.60 V vs Na/Na^+. In addition, the redox peaks of the $Ni^{2+/3+/4+}$ species show a minor peak splitting, appearing as a weak shoulder or a dip within the primary redox feature, and do not indicate the formation of a separate redox couple. For NFMNi0.1, NFMNi0.05, NFMNi0.02, and NFMO, only the Mn^{3+}/Mn^{4+} redox pair is visible at 2.51/1.81, 2.77/1.85, 2.55/1.86, and 2.74/1.87 V vs Na/Na^+. In the extended potential range of 1.5 to 4.2 V, NMNiO exhibits the same redox reactions as observed between 1.5 and 4.0 V. However, from 4.1 V onward, the onset of a high-voltage aniodic process is visible as an open-ended current tail up to the 4.2 V limit for all samples. The oxidation peaks corresponding to the redox pairs Mn^{3+}/Mn^{4+}, Ni^{2+}/Ni^{3+}, and Ni^{3+}/Ni^{4+} are observed at 2.12, 3.22/3.37, and 3.69/3.72 V, respectively, while the corresponding reduction peaks are observed at 1.77, 3.09/3.24, and 3.53/3.60 V. Splitting in both $Ni^{2+/3+}$ and $Ni^{3+/4+}$ peaks is again evident. For the NFMNi0.1, NFMNi0.05, and NFMNi0.02 samples, in addition to the Mn^{3+}/Mn^{4+} redox peak in the reduction, another peak is visible that can be attributed to the Fe^{3+}/Fe^{4+} redox pair. This peak is also visible in NFMO but is significantly weaker. The Mn^{3+}/Mn^{4+} peaks are at 2.49/1.79 V (NFMNi0.1), 2.60/1.91 V (NFMNi0.05), 2.50/1.89 V (NFMNi0.02), and 2.72/1.86 V (NFMO) vs Na/Na^+, whereas the Fe^{3+}/Fe^{4+} reduction peak can be found at higher potentials at 3.66, 3.58, 3.56, and 3.55 V vs Na/Na^+.[21,48,49]

The splitting of both $Ni^{2+/3+}$ and $Ni^{3+/4+}$ peaks in NMNiO indicates a rearrangement of the Na^+/vacancies in the Na layer. This rearrangement is due to the superstructure of the honeycomb-shaped Ni/Fe arrangement, which leads to an LZZ Na^+/vacancy order.[27] This phenomenon is observed in both potential windows. It is evident that the higher potential activates the Fe^{3+}/Fe^{4+} redox reaction.[20,48−50] Furthermore, the introduction of Ni into the Fe/Mn system appears to enhance this redox reaction, an effect that has also been described in the literature in connection with Ti or Mg substitution.[21,49] However, only weak Fe redox activity is observed

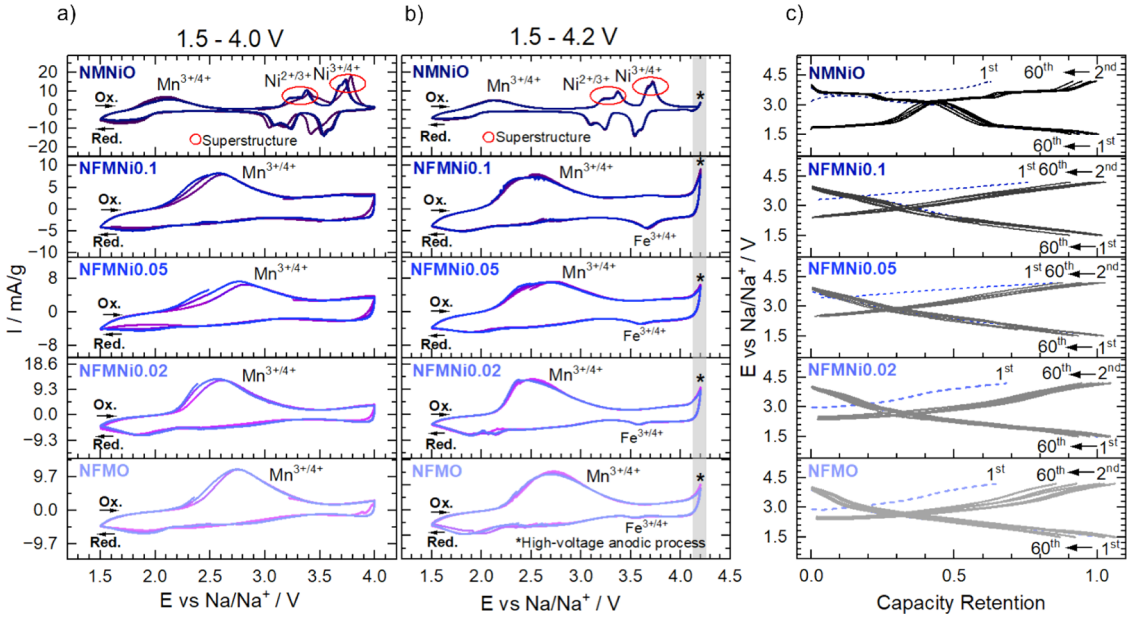

Figure 5. CV of P2-$Na_{0.66}Mn_{2/3}Fe_{1/3-x}Ni_x$ (x = 0, 0.02, 0.05, 0.1, and 1/3) between 1.5 and 4.0 V (a) and 1.5 and 4.2 V vs Na/Na^+ (b). Galvanostatic charge/discharge profiles of P2-$Na_{0.66}Mn_{2/3}Fe_{1/3-x}Ni_x$ (x = 0, 0.02, 0.05, 0.1, and 1/3) between 1.5 and 4.2 V vs Na/Na^+(c).

https://doi.org/10.1021/acsaem.6c02501
ACS Appl. Energy Mater. 2026, 9, 13655−13667

Downloaded from pubs.acs.org/aaemcq/article-pdf/9/20/13655/6878184/ae-2026-02501p.pdf by RWTH AACHEN HOCHSCHUL BIBL user on 10 November 2026

in the Fe/Mn system, which is significantly lower than in the trimetallic system. This confirms once again that the substitution of a third metal can enhance or activate the Fe^{3+}/Fe^{4+} redox reaction. The high-potential oxidation feature observed in all samples during cycling up to 4.2 V vs Na/Na^+ can be attributed to the oxidation of lattice oxygen in the material itself, the onset of phase transformation from P2 to O2, or the decomposition of the electrolyte.[7] In addition, in all samples except NMNiO, the main redox pair is Mn^{3+}/Mn^{4+}. At higher potentials, the redox pair Fe^{3+}/Fe^{4+} also contributes to the overall reaction, whereby its contribution increases with increasing Ni concentration. Ni, on the other hand, shows no significant electrochemical activity in the Ni/Fe/Mn system.

Galvanostatic charge/discharge measurements exhibited a systematic change with increasing Ni content, which is consistent with the observations in CV (Figure 5c). NMNiO exhibits characteristic, multistep voltage curves during charging and discharging. Initially, a plateau occurs in the range of 1.86–2.12 and 3.10–3.36 V vs Na/Na^+ followed by another plateau between 3.60 and 3.74 V vs Na/Na^+. In contrast, the ternary systems exhibit charging/discharging profiles that are significantly smoother. The presence of pronounced plateaus that were previously observed has now diminished.

Multistep charge/discharge profiles indicate the presence of different Na^+/vacancy arrangements within the layers. As evidenced by PXRD, Raman, and FTIR analysis and in agreement with the literature-documented findings regarding TM doping in layered oxides, the incorporation of Fe into the Mn/Ni-based system disrupts the Na^+/vacancy and honeycomb structures, thereby facilitating smoother plateaus for both ternary systems and Mn/Fe-based system.[4,25,27,37] Furthermore, the observations point toward a stronger structural degradation in the Mn/Fe-based system, which implies that the ternary systems maintain better structural integrity.[15,27] To further investigate the structural behavior of the material during cycling, *in situ* XRD measurements were conducted.

3.4. *In Situ* XRD

To understand the influence of the Fe/Mn/Ni ratio on the structural behavior during sodiation/desodiation, *in situ* XRD measurements in half-cells between 1.5 and 4.2 V vs Na/Na^+ were conducted (Figure 6 and Figure S5 in the Supporting Information). The Rietveld refinement reveals different phase evolution profiles within the potential window for the five samples, ranging from the coexistence of P2 and P′2 to the complete transformation of P2 into P′2. However, clear shifts in the

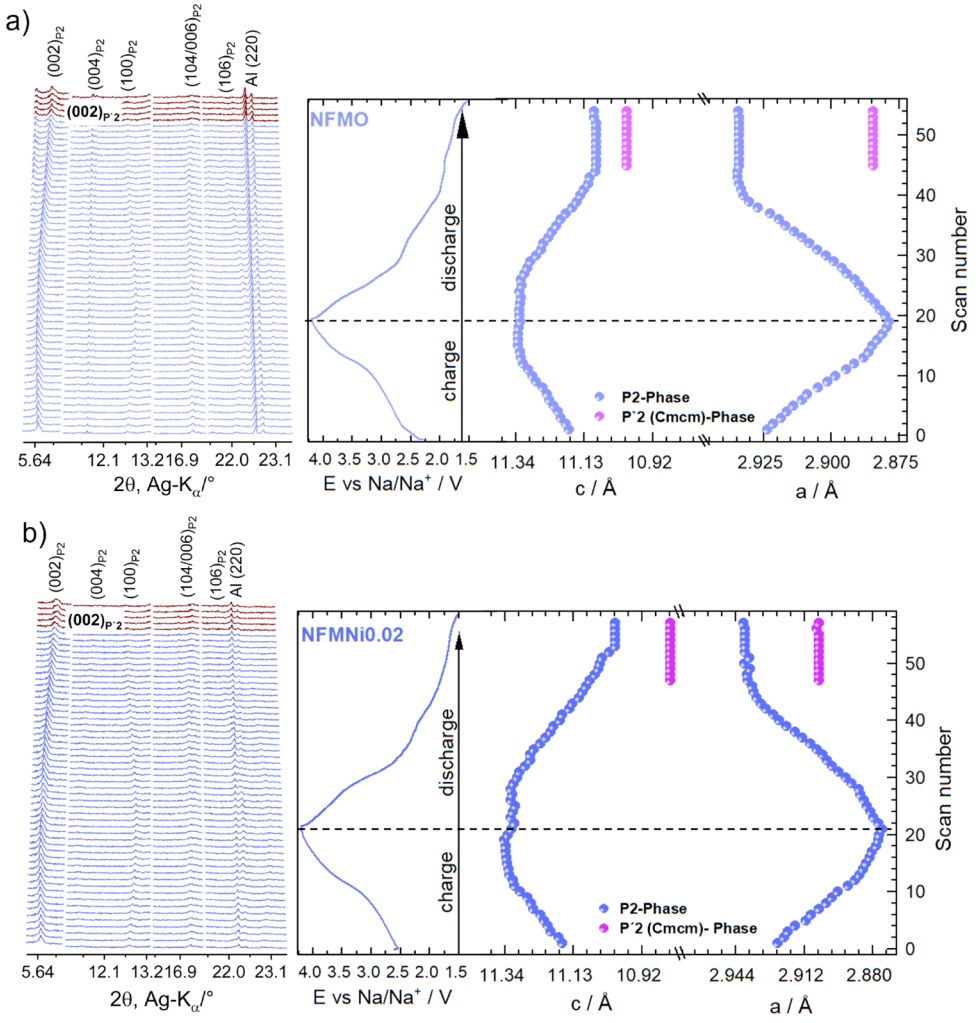

Figure 6. Waterfall diagram of XRD scans during cycling and determined lattice parameters a_{hex} and c_{hex} of *in situ* XRD measurements in P2-$Na_{0.66}Mn_{2/3}Fe_{1/3-x}Ni_x$, $x = 0$ (a) and 0.02 (b).

https://doi.org/10.1021/acsaem.6c02501
ACS Appl. Energy Mater. 2026, 9, 13655−13667

Downloaded from pubs.acs.org/aaemcq/article-pdf/9/20/13655/6878184/ae-2026-02501p.pdf by RWTH AACHEN HOCHSCHUL BIBL user on 10 November 2026

(002), (004), (100), and (104) reflections are visible, indicating changes in oxidation states Mn^{3+}/Mn^{4+}, Fe^{2+}/Fe^{3+}, and $Ni^{2+}/Ni^{3+}/Ni^{4+}$, respectively. The observed decrease in a_{hex} and concurrent increase in c_{hex} during charging can be ascribed to TM oxidation, leading to smaller ionic radii, and the removal of Na^+ ions from the layer, which enhances electrostatic repulsion between the layers.

A comparison of the lattice parameter changes upon cycling shows a clear compositional trend. NFMO exhibits lattice variations of $a_{hex} = 1.99\%$ and $c_{hex} = 2.10\%$, which increase with Ni substitution to $a_{hex} = 2.22\%$ and $c_{hex} = 3.02\%$ for NFMNi0.02 and further to $a_{hex} = 2.44\%$ and $c_{hex} = 3.65\%$ for NFMNi0.05. Interestingly, for NFMNi0.1 the lattice parameter changes decrease again to $a_{hex} = 1.93\%$ and $c_{hex} = 2.35\%$ before reaching the largest expansion in NMNiO with $a_{hex} = 3.51\%$ and $c_{hex} = 4.43\%$.

With increasing Ni content, both a_{hex} and c_{hex} initially increase up to $x = 0.05$, which can be attributed to the increased structural disorder in the TM layer, causing greater changes in TM–O bond lengths and interlayer electrostatics. This effect is therefore attributable to both the intercalation of a larger Ni^{2+} ion and a higher lattice distortion due to Ni substitution. NFMNi0.1 appears to be a special case, as it exhibits the smallest overall changes in lattice parameters of all samples. This behavior indicates the existence of an optimized composition at a concentration of $x = 0.1$, where the Jahn–Teller distortion of the Mn^{3+} ions might be partially suppressed by the intercalation of Ni. The Ni content is insufficient to induce lattice contraction by Ni^{4+} ions or TM ordering. In addition, the redox pairs are more evenly distributed between Mn^{3+}/Mn^{4+} and Fe^{2+}/Fe^{3+}. This may result in a more continuous redox reaction during sodiation/desodiation. In contrast, the Ni/Mn system exhibits the greatest expansion of both lattice parameters even though it contains less Jahn–Teller active ions compared to NFMO or the ternary compositions. This could be attributed to the presence of a honeycomb superstructure that is disrupted during cycling, leading to voltage jumps and abrupt, step-like changes in the lattice parameters. In addition, the redox reaction in Ni/Mn involves the oxidation states $Ni^{2+}/Ni^{3+}/Ni^{4+}$, and thus, the formation of Ni^{4+} (VI), which has a very small ionic radius (0.48 Å), leads to a significant shortening of the Ni–O bonds, resulting in a strong contraction in the plane. At the same time, the increased charge within the TM–O layers enhances the electrostatic repulsion between neighboring oxygen layers, leading to a pronounced expansion of the *c* axis.

In the deep discharge region below 2 V, the formation of the orthorhombic P′2 phase (*Cmcm*) occurs resulting from the reduction of Mn^{4+} to high-spin Mn^{3+} ($3d^4$) accompanied by Jahn–Teller distortion. Interestingly, for NFMNi0.05, NFMNi0.1, and NMNiO, the P′2 phase is not observed, indicating that the P2 to P′2 phase transition is effectively suppressed, contributing to improved structural stability. Moreover, these findings demonstrate that the integration of Ni into Fe/Mn-based LTMO, even in minor quantities, effectively suppresses the undesirable phase transformation in the deep discharge range. This suppression of phase transformation results from a weakening of the Jahn–Teller distortion and leads to a potential improvement in cycling stability.

Quantification of the *in situ* XRD measurements of NFMO and NFMNi0.02 reveals that, after discharge to 1.5 V, the P2 phase is not completely converted into the P′2 phase; however, an equal ratio of P2 and P′2 is observed at the end of the cycle (Figure 7a,b). After increasing the Ni concentration to $x \geq 0.05$ including the binary Ni/Mn system, the formation of the P′2 phase is suppressed and 100% of the P2 phase is present (Figure 7c).

The observed phase behavior for NFMO can be explained by the fact that a high voltage (cutoff 4.2 V) leads to enhanced Na^+ extraction, which has the potential to induce structural instability, as documented in the literature as reconstructive stacking conversions of OP4 or Z.[51] Despite the absence of direct detection of such phases in the Rietveld refinement, the results indicate the occurrence of local stacking faults and irreversible structural defects, which could potentially trigger this transformation. However, a low Ni concentration of $x = 0.02$ does not appear to have a significant influence on the phase behavior, as no differences are apparent compared to NFMO and a ratio of roughly 1:1 is present for both. This suggests that a Ni concentration of $x = 0.02$ is not sufficient to reduce the amount of Mn^{3+} and prevent a P′2 phase transition. It has been demonstrated that Fe ions have the capability to migrate to tetrahedral interlayer sites,[51] which could partially suppress the complete transformation to the P′2 phase during the discharge process to 1.5 V, resulting in the coexistence of P′2 and P2 phases. At a concentration of $x = 0.05$ Ni in the P2 structure, the proportion of Jahn–Teller active Mn^{3+} ions appear to be sufficiently reduced to completely suppress the undesirable P′2 phase, which could significantly stabilize the phase transition and lead to an improved long-term performance.

4. CONCLUSIONS

In this study the influence of various Fe/Mn/Ni ratios, which are linked to the Mn^{3+}/Mn^{4+} proportions, was investigated in P2-$Na_{0.66}Mn_{2/3}Fe_{1/3-x}Ni_x$ ($x = 0$, 0.02, 0.05, 0.1, and 1/3).

Although ICP-OES revealed a nonlinear trend in the Na content of the samples, suggesting that the Mn^{3+} fraction does not decrease proportionally with increasing Ni^{2+} substitution, the

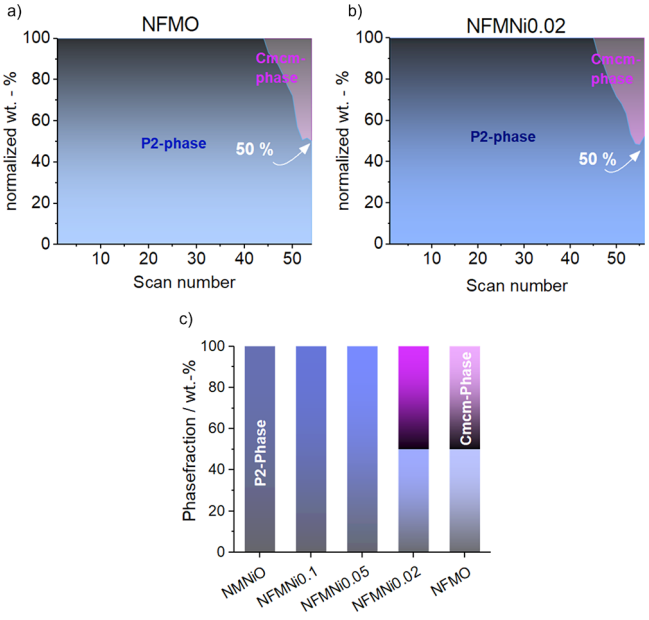

Figure 7. Phase fraction of NFMO (a) and NFMNi0.02 (b) cycled between 1.5 and 4.2 V vs Na/Na^+. Overview of all quantified samples from *in situ* XRD measurement (c).

Downloaded from pubs.acs.org/aaemcq/article-pdf/9/20/13655/6878184/ae-2026-02501p.pdf by RWTH AACHEN HOCHSCHUL BIBL user on 10 November 2026

https://doi.org/10.1021/acsaem.6c02501
ACS Appl. Energy Mater. 2026, 9, 13655−13667

FTIR, PXRD, and EPR results indicate a different trend. FTIR spectroscopy reveals the formation of NaOH and Na_2CO_3 in all samples, suggesting that the Na content determined by ICP-OES cannot be clearly distinguished between Na incorporated into the P2 lattice and Na present as surface species ($NaOH/Na_2CO_3$). Furthermore, PXRD shows a significant decrease in the lattice parameters a_{hex} and c_{hex} with increasing Ni^{2+} substitution. This trend can be attributed to a decreasing Mn^{3+} content and the associated changes in the average cation radii. The PXRD results are further supported by the EPR measurements, which show a progressive narrowing of the linewidth with increasing Ni^{2+} substitution. This behavior indicates an increasing Mn^{4+} content and a corresponding decrease in Mn^{3+}. Since Mn^{4+} is the dominant EPR-active species at room temperature, the increasing Mn^{4+} content is consistent with the observed narrowing of the EPR linewidth.

Moreover, complementary PXRD, Raman, and FTIR measurements reveal distinct structural behaviors in the two binary systems. In the Ni/Mn system, the formation of a superstructure is observed, characterized by a honeycomb-like ordering of the TM cations. Furthermore, disruption of this superstructure occurs during the cycling process, leading to step-like voltage changes that could impair electrochemical performance. With the introduction of Fe into the system, the superstructure is completely disrupted, and the charge/discharge profiles become smoother, indicating a more stable structure in the ternary system.

In situ XRD analysis revealed no detectable phase transformation to the O2 or OP4/Z phase within the potential window 1.5–4.2 V vs Na/Na^+ for all five samples. However, quantitative analysis shows that the Fe/Mn/Ni ratio influences the relative fraction of P2 and P′2 during this low-voltage phase transition. In particular, the P2-to-P′2 conversion is partially suppressed in NFMO and NFMNi0.02, resulting in an equally distributed phase ratio. For $x \geq 0.05$, the formation of the P′2 phase is completely suppressed, and a single P2 phase is maintained throughout the entire potential window. This indicates that a Ni content of $x = 0.02$ is insufficient to reduce the concentration of Jahn–Teller active Mn^{3+} cations and to suppress the undesired phase transition. In contrast, at $x = 0.05$, the P′2 phase is suppressed, demonstrating that even a small increase in Ni content is sufficient to stabilize the lattice.

■ ASSOCIATED CONTENT

Data Availability Statement

Data related to this study are available in the repository at the following link: https://doi.org/10.26165/JUELICH-DATA/MXHMFS.

Supporting Information

The Supporting Information is available free of charge at https://pubs.acs.org/doi/10.1021/acsaem.6c02501.

ICP-OES; Rietveld refinement of PXRD of NFMNi0.02, 0.05, and 0.1; determined lattice parameters; determined distances of EXFAS; Raman band positions; Fe/Ni proportion; X-Band EPR spectrum MnO_2; capacities; and *in situ* XRD of NFMNi0.05, 0.01 and NMNiO (DOCX)

■ AUTHOR INFORMATION

Corresponding Author

Anna Domgans – *Institute for Energy Technologies (IET-1 Fundamental Electrochemistry), Forschungszentrum Jülich, Jülich 52428, Germany; Material and Processes of Electrochemical Energy Storage and Conversion, RWTH Aachen University, Aachen 52425, Germany;* orcid.org/0009-0004-9879-2700; Email: a.domgans@fz-juelich.de

Authors

Tobias Braun – *Institute for Energy Technologies (IET-1 Fundamental Electrochemistry), Forschungszentrum Jülich, Jülich 52428, Germany; Material and Processes of Electrochemical Energy Storage and Conversion, RWTH Aachen University, Aachen 52425, Germany*

Davis Thomas Daniel – *Institute for Energy Technologies (IET-1 Fundamental Electrochemistry), Forschungszentrum Jülich, Jülich 52428, Germany;* orcid.org/0000-0001-7035-3416

Nabi Aghdassi – *Institute for Energy Technologies (IET-1 Fundamental Electrochemistry), Forschungszentrum Jülich, Jülich 52428, Germany*

Sebastian Speer – *Institute for Energy Technologies (IET-1 Fundamental Electrochemistry), Forschungszentrum Jülich, Jülich 52428, Germany; Material and Processes of Electrochemical Energy Storage and Conversion, RWTH Aachen University, Aachen 52425, Germany*

Andre Rossberg – *Institute of Resource Ecology, Helmholtz Zentrum Dresden Rossendorf, Dresden 01328, Germany; European Synchrotron Radiation Facility, The Rossendorf Beamline, Grenoble 38043, France*

Sebastian Schumacher – *Institute for Energy Technologies (IET-1 Fundamental Electrochemistry), Forschungszentrum Jülich, Jülich 52428, Germany; Material and Processes of Electrochemical Energy Storage and Conversion, RWTH Aachen University, Aachen 52425, Germany*

Evgeny V. Alekseev – *Institute for Energy Technologies (IET-1 Fundamental Electrochemistry), Forschungszentrum Jülich, Jülich 52428, Germany;* orcid.org/0000-0002-4919-5211

Luc Raijmakers – *Institute for Energy Technologies (IET-1 Fundamental Electrochemistry), Forschungszentrum Jülich, Jülich 52428, Germany*

Anna Windmüller – *Institute for Energy Technologies (IET-1 Fundamental Electrochemistry), Forschungszentrum Jülich, Jülich 52428, Germany;* orcid.org/0000-0003-2829-3362

Rüdiger-A. Eichel – *Institute for Energy Technologies (IET-1 Fundamental Electrochemistry), Forschungszentrum Jülich, Jülich 52428, Germany; Material and Processes of Electrochemical Energy Storage and Conversion, RWTH Aachen University, Aachen 52425, Germany;* orcid.org/0000-0002-0013-6325

Complete contact information is available at: https://pubs.acs.org/doi/10.1021/acsaem.6c02501

Author Contributions

‡A.D. and T.B. contributed equally to this work.

Notes

The authors declare no competing financial interest.

■ ACKNOWLEDGMENTS

This work was financially supported by the project of "High Performance Solid-State Batteries" (HIPSTER) from

Downloaded from pubs.acs.org/aaemcq/article-pdf/9/20/13655/6878184/ae-2026-02501p.pdf by RWTH AACHEN HOCHSCHUL BIBL user on 10 November 2026

"Ministerium für Kultur und Wissenschaft des Landes Nordrhein-Westfalen" and from "Bundesministerium für Bildung und Forschung".

REFERENCES

(1) Wang, P.-F.; Yao, H.-R.; Liu, X.-Y.; Yin, Y.-X.; Zhang, J.-N.; Wen, Y.; Yu, X.; Gu, L.; Guo, Y.-G. Na^+/vacancy disordering promises high-rate Na-ion batteries. *Sci. Adv.* **2018**, *4*.

(2) Chen, T.; Ouyang, B.; Fan, X.; Zhou, W.; Liu, W.; Liu, K. Oxide cathodes for sodium-ion batteries: Designs, challenges, and perspectives. *Carbon Energy* **2022**, *4* (2), 170–199.

(3) Durmus, Y. E.; Zhang, H.; Baakes, F.; Desmaizieres, G.; Hayun, H.; Yang, L.; Kolek, M.; Küpers, V.; Janek, J.; Mandler, D.; Passerini, S.; Ein-Eli, Y. Side by Side Battery Technologies with Lithium-Ion Based Batteries. *Adv. Energy Mater.* **2020**, *10* (24). No. 2000089.

(4) Chen, Y.; Su, G.; Cheng, X.; Du, T.; Han, Y.; Qiang, W.; Huang, B. Electrochemical performances of P2-$Na_{2/3}Ni_{1/3}Mn_{2/3}O_2$ doped with Li and Mg for high cycle stability. *J. Alloys Compd.* **2021**, *858*, No. 157717.

(5) Liu, Y.; Zhang, Y.-H.; Ma, J.; Zhao, J.; Li, X.; Cui, G. Challenges and Strategies toward Practical Application of Layered Transition Metal Oxide Cathodes for Sodium-Ion Batteries. *Chem. Mater.* **2024**, *36* (1), 54–73.

(6) Zhang, J.; Wang, W.; Wang, W.; Wang, S.; Li, B. Comprehensive Review of P2-Type $Na_{2/3}Ni_{1/3}Mn_{2/3}O_2$, a Potential Cathode for Practical Application of Na-Ion Batteries. *ACS Appl. Mater. Interfaces* **2019**, *11* (25), 22051–22066.

(7) Zhong, X.-B.; He, C.; Gao, F.; Tian, Z.-Q.; Li, J.-F. In situ Raman spectroscopy reveals the mechanism of titanium substitution in P2–$Na_{2/3}Ni_{1/3}Mn_{2/3}O_2$: Cathode materials for sodium batteries. *J. Energy Chem.* **2021**, *53*, 323–328.

(8) Kim, H. Sodium-Ion Battery: Can It Compete with Li-Ion? *ACS Mater. Au* **2023**, *3* (6), 571–575.

(9) Peng, B.; Zhou, Z.; Shi, J.; Huang, X.; Li, Y.; Ma, L. Earth-Abundant Fe-Mn-Based Compound Cathodes for Sodium-Ion Batteries: Challenges and Progress. *Adv. Funct. Mater.* **2024**, *34* (19), No. 2311816.

(10) Delmas, C.; Fouassier, C.; Hagenmüller, P. Structural classification and properties of the layered oxides. *Physica* **1980**, *99*, 81–85.

(11) Yabuuchi, N.; Yano, M.; Yoshida, H.; Kuze, S.; Komaba, S. Synthesis and Electrode Performance of O_3-Type $NaFeO_2$-$NaNi_{1/2}Mn_{1/2}O_2$ Solid Solution for Rechargeable Sodium Batteries. *J. Electrochem. Soc.* **2013**, *160* (5), A3131–A3137.

(12) Kubota, K.; Miyazaki, M.; Kim, E. J.; Yoshida, H.; Barpanda, P.; Komaba, S. Structural change induced by electrochemical sodium extraction from layered O′3-$NaMnO_2$. *J. Mater. Chem. A* **2021**, *9* (47), 26810–26819.

(13) Steele, J. M. A.; Bocarsly, J. D.; Nagle-Cocco, L. A. V.; Phillips, G. S.; Sayed, F. N.; Lampronti, G. I.; Orlandi, F.; Manuel, P.; Mikulska, I.; Grey, C. P.; Dutton, S. E. Evolution of Charge and Orbital Ordering, and Cation Vacancy Ordering During Electrochemical Desodiation of Na_xNiO_2. *J. Am. Chem. Soc.* **2026**, *148* (21), 22062–22076.

(14) Zhao, Y.; Liu, Q.; Zhao, X.; Mu, D.; Tan, G.; Li, L.; Chen, R.; Wu, F. Structure evolution of layered transition metal oxide cathode materials for Na-ion batteries: Issues, mechanism and strategies. *Mater. Today* **2023**, *62*, 271–295.

(15) Somerville, J. W.; Sobkowiak, A.; Tapia-Ruiz, N.; Billaud, J.; Lozano, J. G.; House, R. A.; Gallington, L. C.; Ericsson, T.; Häggström, L.; Roberts, M. R.; Maitra, U.; Bruce, P. G. Nature of the "Z"-phase in layered Na-ion battery cathodes. *Energy Environ. Sci.* **2019**, *12* (7), 2223–2232.

(16) Ding, C.; Nohira, T.; Hagiwara, R. Charge-discharge performance of $Na_{2/3}Fe_{1/3}Mn_{2/3}O_2$ positive electrode in an ionic liquid electrolyte at 90 °C for sodium secondary batteries. *Electrochim. Acta* **2017**, *231*, 412–416.

(17) Forero-Saboya, J.; Zhou, Y.; Browne, S.; Moiseev, I. A.; Pablos, C.; Abou-Rjeily, J.; Mboup, A.; Alphen, C.; Zhang, L.; Li, B.; Abakumov, A. M.; Tarascon, J.-M.; Mariyappan, S. O3- vs P2-type $Na_x(Ni,Zn,Mn,Ti)O_2$ layered oxides: Comparative study on electrode-electrolyte reactivity and structural stability for cycling performance. *Energy Storage Mater.* **2025**, *80*, No. 104423.

(18) Chang, L.; Yang, R.; Bi, X.; Yang, W.; Cai, K.; Wei, A.; Liu, J. Research progress of layered P2-$Na_{2/3}Ni_{1/3}Mn_{2/3}O_2$ cathode material for sodium ion batteries. *J. Energy Storage* **2023**, *73*, No. 109025.

(19) Lee, D. H.; Xu, J.; Meng, Y. S. An advanced cathode for Na-ion batteries with high rate and excellent structural stability. *Phys. Chem. Chem. Phys.* **2013**, *15* (9), 3304–3312.

(20) Zhao, J.; Xu, J.; Lee, D. H.; Dimov, N.; Meng, Y. S.; Okada, S. Electrochemical and thermal properties of P2-type $Na_{2/3}Fe_{1/3}Mn_{2/3}O_2$ for Na-ion batteries. *J. Power Sources* **2014**, *264*, 235–239.

(21) Yang, T.; Huang, Y.; Zhang, J.; Zhu, H.; Ren, J.; Li, T.; Gallington, L. C.; Lan, S.; Yang, L.; Liu, Q. Insights into Ti doping for stabilizing the $Na_{2/3}Fe_{1/3}Mn_{2/3}O_2$ cathode in sodium ion battery. *J. Energy Chem.* **2022**, *73*, 542–548.

(22) Zhou, P.; Zhang, J.; Che, Z.; Quan, Z.; Duan, J.; Wu, X.; Weng, J.; Zhao, J.; Zhou, J. Insights into the enhanced structure stability and electrochemical performance of Ti^{4+}/F^- co-doped P2-$Na_{0.67}Ni_{0.33}Mn_{0.67}O_2$ cathodes for sodium ion batteries at high voltage. *J. Energy Chem.* **2022**, *67*, 655–662.

(23) Gutierrez, A.; Dose, W. M.; Borkiewicz, O.; Guo, F.; Avdeev, M.; Kim, S.; Fister, T. T.; Ren, Y.; Bareño, J.; Johnson, C. S. On Disrupting the Na^+-Ion/Vacancy Ordering in P2-Type Sodium–Manganese–Nickel Oxide Cathodes for Na^+-Ion Batteries. *J. Phys. Chem. C* **2018**, *122* (41), 23251–23260.

(24) Pfeiffer, L. F.; Dillenz, M.; Burgard, N.; Beran, P.; Roscher, D.; Zarrabeitia, M.; Drews, P.; Hervoches, C.; Mikhailova, D.; Omar, A.; Baran, V.; Paul, N.; Sotoudeh, M.; Busch, M.; Wohlfahrt-Mehrens, M.; Groß, A.; Passerini, S.; Axmann, P. From structure to electrochemistry: the influence of transition metal ordering on Na^+ /vacancy orderings in P2-type Na_x MO_2 cathode materials for sodium-ion batteries. *J. Mater. Chem. A* **2024**, *13* (1), 540–560.

(25) Yao, H.-R.; Lv, W.-J.; Yuan, X.-G.; Guo, Y.-J.; Zheng, L.; Yang, X.-A.; Li, J.; Huang, Y.; Huang, Z.; Wang, P.-F.; Guo, Y.-G. New insights to build Na^+/vacancy disordering for high-performance P2-type layered oxide cathodes. *Nano Energy* **2022**, *97*, No. 107207.

(26) Laisa, C. P.; Nanda Kumar, A. K.; Selva Chandrasekaran, S.; Murugan, P.; Lakshminarasimhan, N.; Govindaraj, R.; Ramesha, K. A comparative study on electrochemical cycling stability of lithium rich layered cathode materials $Li_{1.2}Ni_{0.13}M_{0.13}Mn_{0.54}O_2$ where M═Fe or Co. *J. Power Sources* **2016**, *324*, 462–474.

(27) Yang, Q.; Wang, P.-F.; Guo, J.-Z.; Chen, Z.-M.; Pang, W.-L.; Huang, K.-C.; Guo, Y.-G.; Wu, X.-L.; Zhang, J.-P. Advanced P2-$Na_{2/3}Ni_{1/3}Mn_{7/12}Fe_{1/12}O_2$ Cathode Material with Suppressed P2-O2 Phase Transition toward High-Performance Sodium-Ion Battery. *ACS Appl. Mater. Interfaces* **2018**, *10* (40), 34272–34282.

(28) Domgans, A.; Tran, N. T. T.; Speer, S.; Kayani, A. N.; Zantis, F.; Braun, T.; Schaps, K.; Tsai, C.-L.; Tempel, H.; Raijmakers, L.; Lin, S.; Windmüller, A.; Eichel, R.-A. Selective Halide Incorporation in P2-$Na_{0.66}Fe_{1/3}Mn_{2/3}O_2$ Cathodes: Revealing a Compositional Regime for Enhanced Cycling. *Small Struct.* **2026**, *7* (2), No. e202500808 .

(29) Mortemard de Boisse, B.; Carlier, D.; Guignard, M.; Guerin, E.; Duttine, M.; Wattiaux, A.; Delmas, C. Influence of Mn/Fe Ratio on Electrochemical and Structural Properties of P2-$Na_xMn_{1-y}Fe_yO_2$ Phases as Positive Electrode Material for Na-Ion Batteries. *Chem. Mater.* **2018**, *30* (21), 7672–7681.

(30) Scheinost, A. C.; Claussner, J.; Exner, J.; Feig, M.; Findeisen, S.; Hennig, C.; Kvashnina, K. O.; Naudet, D.; Prieur, D.; Rossberg, A.; Schmidt, M.; Qiu, C.; Colomp, P.; Cohen, C.; Dettona, E.; Dyadkin, V.; Stumpf, T. ROBL-II at ESRF: a synchrotron toolbox for actinide research. *J. Synchrotron Radiat.* **2021**, *28* (Pt 1), 333–349.

(31) Ankudinov, A. L.; Ravel, B.; Rehr, J. J.; Conradson, S. D. Real-space multiple-scattering calculation and interpretation of x-ray-absorption near-edge structure. *Phys. Rev. B* **1998**, *58* (12), 7565–7576.

(32) Singh, G.; Del López Amo, J. M.; Galceran, M.; Pérez-Villar, S.; Rojo, T. Structural evolution during sodium deintercalation/

Downloaded from pubs.acs.org/aaemcq/article-pdf/9/20/13655/6878184/aae-2026-02501p.pdf by RWTH AACHEN HOCHSCHUL BIBL user on 10 November 2026

https://doi.org/10.1021/acsaem.6c02501
ACS Appl. Energy Mater. 2026, 9, 13655–13667

intercalation in $Na_{2/3}[Fe_{1/2}Mn_{1/2}]O_2$. *J. Mater. Chem. A* **2015**, *3* (13), 6954–6961.
(33) Pawley, G. S. EDINP, the Edinburgh powder profile refinement program. *J. Appl. Cryst.* **1980**, *13*, 630–633.
(34) Paulsen, J. M.; J. D. Studies of the layered manganese bronzes, $Na_{2/3}[Mn_{1-x}M_x]O_2$ with M=Co, Ni, Li, and $Li_{2/3}[Mn_{1-x}M_x]O_2$ prepared by ion-exchange. *Solid State Ionics* **1999**, *126*, 3–24.
(35) Shi, Y.; Jiang, P.; Wang, S.; Chen, W.; Wei, B.; Lu, X.; Qian, G.; Kan, W. H.; Chen, H.; Yin, W.; Sun, Y.; Lu, X. Slight compositional variation-induced structural disorder-to-order transition enables fast Na^+ storage in layered transition metal oxides. *Nat. Commun.* **2022**, *13* (1), 7888.
(36) Lee, E.; Brown, D. E.; Alp, E. E.; Ren, Y.; Lu, J.; Woo, J.-J.; Johnson, C. S. New Insights into the Performance Degradation of Fe-Based Layered Oxides in Sodium-Ion Batteries: Instability of Fe^{3+}/Fe^{4+} Redox in α-$NaFeO_2$. *Chem. Mater.* **2015**, *27* (19), 6755–6764.
(37) Risthaus, T.; Zhou, D.; Cao, X.; He, X.; Qiu, B.; Wang, J.; Zhang, L.; Liu, Z.; Paillard, E.; Schumacher, G.; Winter, M.; Li, J. A high-capacity P2 $Na_{2/3}Ni_{1/3}Mn_{2/3}O_2$ cathode material for sodium ion batteries with oxygen activity. *J. Power Sources* **2018**, *395*, 16–24.
(38) Zhao, W.; Kirie, H.; Tanaka, A.; Unno, M.; Yamamoto, S.; Noguchi, H. Synthesis of metal ion substituted P2-$Na_{2/3}Ni_{1/3}Mn_{2/3}O_2$ cathode material with enhanced performance for Na ion batteries. *Mater. Lett.* **2014**, *135*, 131–134.
(39) Baumann, M.; Häringer, M.; Schmidt, M.; Schneider, L.; Peters, J. F.; Bauer, W.; Binder, J. R.; Weil, M. Prospective Sustainability Screening of Sodium-Ion Battery Cathode Materials. *Adv. Energy Mater.* **2022**, *12* (46), No. 2202636.
(40) Zuo, W.; Ren, F.; Li, Q.; Wu, X.; Fang, F.; Yu, X.; Li, H.; Yang, Y. Insights of the anionic redox in P2–$Na_{0.67}Ni_{0.33}Mn_{0.67}O_2$. *Nano Energy* **2020**, *78*, No. 105285.
(41) Rahmawati, F.; Kusumaningtyas, A. A.; Saraswati, T. E.; Prasetyo, A.; Suendo, V. Mn-doped $NaFeO_2$ from a low purity-Fe precursor and its performance as cathode for Sodium-Ion Battery. *Inorg. Nano-Met. Chem.* **2021**, *51* (3), 383–390.
(42) Zhao, W.; Tanaka, A.; Tanaka, A.; Unno, M.; Yamamoto, S.; Noguchi, H. Synthesis of $LiNi_{1/3}Mn_{2/3}O_2$ related cathode material from P2-$Na_{2/3}Ni_{1/3}Mn_{2/3}O_2$ for lithium ion battery. *Mat. Lett.* **2014**, *134*, 206–209.
(43) Kakazey, M.; Ivanova, N.; Sokolsky, G.; Gonzalez-Rodriguez, J. G. Electron Paramagnetic Resonance of MnO_2 Powders. *Electrochem. Solid-State Lett.* **2001**, *4*, J1–J5.
(44) Krzystek, J.; Ozarowski, A.; Telser, J. Multi-frequency, high-field EPR as a powerful tool to accurately determine zero-field splitting in high-spin transition metal coordination complexes. *Coord. Chem. Rev.* **2006**, *250* (17–18), 2308–2324.
(45) Stoyanova, R.; Zhecheva, E.; Vassilev, S. Mn^{4+} environment in layered $Li[Mg_{0.5-x}NixMn_{0.5}]O_2$ oxides monitored by EPR spectroscopy. *J. Solid State Chem.* **2006**, *179* (2), 378–388.
(46) Zając, T.; Folcik, L.; Kołodziejczyk, A.; Drulis, H.; Krop, K.; Gritzner, G. Electron spin resonance in iron-substituted manganites $La_{0.67}Ca_{0.33}Mn_{1-x}Fe_xO_3$ *J. Magn. Magn. Mater.* **2004**, *272–276*, 120–121.
(47) Zhang, Y.-Y.; Zhang, S.-J.; Li, J.-T.; Wang, K.; Zhang, Y.-C.; Liu, Q.; Xie, R.-S.; Pei, Y.-R.; Huang, L.; Sun, S.-G. Improvement of electrochemical properties of P2-type $Na_{2/3}Mn_{2/3}Ni_{1/3}O_2$ sodium ion battery cathode material by water-soluble binders. *Electrochim. Acta* **2019**, *298*, 496–504.
(48) Moeez, I.; Susanto, D.; Chang, W.; Lim, H.-D.; Chung, K. Y. Artificial cathode electrolyte interphase by functional additives toward long-life sodium-ion batteries. *Chem. Eng. J.* **2021**, *425*, No. 130547.
(49) Boivin, E.; House, R. A.; Marie, J.-J.; Bruce, P. G. Controlling Iron Versus Oxygen Redox in the Layered Cathode $Na_{0.67}Fe_{0.5}Mn_{0.5}O_2$: Mitigating Voltage and Capacity Fade by Mg Substitution. *Adv. Energy Mater.* **2022**, *12* (30), No. 2200702.
(50) Yuan, Z.; Xuehang, W.; Wenwei, W.; Kaituo, W. Synthesis and electrochemical performance of $Na_{0.7}Fe_{0.7}Mn_{0.3}O_2$ as a cathode material for Na-ion battery. *Ceram. Int.* **2014**, *40* (8), 13679–13682.
(51) Talaie, E.; Duffort, V.; Smith, H. L.; Fultz, B.; Nazar, L. F. Structure of the high voltage phase of layered P2-$Na_{2/3-z}[Mn_{1/2}Fe_{1/2}]O_2$ and the positive effect of Ni substitution on its stability. *Energy Environ. Sci.* **2015**, *8* (8), 2512–2523.

Downloaded from pubs.acs.org/aaemcq/article-pdf/9/20/13655/6878184/ae-2026-02501p.pdf by RWTH AACHEN HOCHSCHUL BIBL user on 10 November 2026

https://doi.org/10.1021/acsaem.6c02501
ACS Appl. Energy Mater. 2026, 9, 13655–13667